Scattering Properties of Argon Gas in the Temperature Range 87.3–120 K

I.F. Al-Maaitah[a], B.R. Joudeh[a,b,*], A.S. Sandouqa[c] and H.B. Ghassib[d]

[a]Applied Physics Department, Faculty of Science, Tafila Technical University, Tafila, Jordan

[b]Department of Computer Science, College of Shari'a and Islamic Studies in Al Ahsaa,
Al Imam Muhammad Ibn Saud Islamic University (IMSIU), Saudi Arabia

[c]Department of Physics, Faculty of Engineering Technology, Al-Balqa' Applied University, Amman, Jordan

[d]Department of Physics, Faculty of Science, The University of Jordan, Amman, Jordan

A theoretical model, based on the Galitskii–Migdal–Feynman formalism, is introduced for determining the scattering properties of argon gas, especially the "effective" total, viscosity and average cross-sections. The effective phase shifts are used to compute the quantum second virial coefficient in the temperature range 87.3–120 K. The sole input is the Hartree–Fock dispersion (HFD-B3) potential. The thermophysical properties of the gas are then calculated. The results are in good agreement with experimental data.

1. Introduction

Scientific interest in argon has arisen because of its molecular simplicity. Since the molecule is monoatomic, nonpolar and completely spherical, argon gas is commonly used as a reference fluid to establish and test molecular approaches for predicting thermodynamic properties and for calibrating new apparatuses for thermodynamic measurements [1]. In addition, argon is a model substance for fundamental atomic and condensed matter physics. This substance has been the subject of numerous experimental and theoretical investigations. Thanks to its relative cheapness, commercial and industrial applications of argon are widespread [1, 2].

Many theoretical methods have been developed for studying the properties of argon gas: Monte Carlo simulations [3] were used to predict the thermophysical properties of pure Ar as well as the binary mixtures Ne–Ar. An *ab initio* potential was used in computer simulations to yield the thermodynamic properties of the fluid phases [4]. The effective diameters and free volumes of argon were evaluated over a wide range of densities and temperatures. The thermophysical properties of the gas were evaluated from 83 to 10000 K, using quantum-mechanical *ab initio* calculations. The calculated quantities included the second pressure virial coefficient, second acoustic virial coefficient, second dielectric virial coefficient as well as viscosity and thermal conductivity [5].

An analytic equation of state, based on a statistical-mechanical perturbation theory, was applied to calculate the thermodynamic properties of the gas. These included the vapor pressure curve, compressibility factor,

fugacity coefficient [1], internal energy, enthalpy, entropy and heat capacity [6], using a Lennard-Jones (12-6)-type potential. The density, internal energy, enthalpy, entropy, specific heat, compressibility factor as well as second virial and the Joule–Thomson coefficients of liquid and gaseous argon were determined in the temperature range 83.8–300 K at pressures 0.01–1000 atm [7].

An equation of state for argon has been written in terms of the reduced Helmholtz free energy [8]. This equation incorporates a substantive amount of experimental thermodynamic data. It covers the largest part of the fluid region and is valid for single-phase and saturation states from the melting line to 700 K at pressures up to 1000 MPa. Another recent equation of state for argon has been developed [9]. This new equation has been derived from the measured heat capacity $CV(\rho, T)$ and pressure $P(\rho, T)$. It is valid for the whole fluid region (single-phase and coexistence states) from the melting line to 2300 K and for pressures up to 50 000 MPa. It shows a more physical behavior along isochors when T tends to zero for such basic properties as the isochoric heat capacity and the compressibility factor. It also displays a more reasonable behavior for the crossing of the coexistence phase.

In this paper, the Galitskii–Migdal–Feynman (GMF) formalism [10–14] is applied to Ar gas for studying its scattering and thermodynamic properties in the temperature range 87.3–120 K, using the Hartree–Fock dispersion (HFD-B3) interatomic potential, with special emphasis on the quantum second virial coefficient [15]. The validity of the GMF formalism in the low-density regime has been demonstrated repeatedly over the years [10–14]. The reason for this choice of temperature range is to enable us to compare our results to other results available in the literature, both experimental and theoretical. In this range, Ar gas furnishes a fertile ground for applying many-body

*corresponding author; e-mail: brjoudeh.bj@gmail.com

formalisms of the type used here — i.e., formalisms which operate best for relatively low-dense (in the sense that the interaction range is less than the interparticle spacing), weakly-interacting systems.

The lower-temperature limit (87.3 K) is close to the boiling point of Ar. By the time the system reaches the higher limit (120 K), it is already very much a gas, though still a nonideal fluid, with some residual "quantumness" — the "quantum" character and nonideality diminishing gradually with increasing temperature. Thus, we have here a nonideal gas which is a fertile ground for applying many-body formalisms of the type used in this work.

The basic quantity in the GMF formalism is the T-matrix. It is essentially an "effective" pairwise interaction in momentum space which takes into account the presence of the many-body medium in some average manner. It can also be viewed as a generalized scattering amplitude, or as a "dressed" Lippmann–Schwinger t-matrix (which describes the scattering of two particles in free space). The GMF T-matrix was originally derived for many-fermionic systems, but was later adapted to many-bosonic systems [12, 13]. This formalism is used to calculate the "effective" phase shifts that incorporate many-body effects; they are functions of the density and temperature. From these phase shifts all other properties of the system follow.

The rest of the paper is organized as follows. The theoretical framework is presented in Sect. 2. The results are summarized and discussed in Sect. 3. Finally, in Sect. 4, the paper is concluded with some closing remarks.

2. Theoretical framework

2.1. Effective cross-sections

We start with boson–boson scattering in a medium. A spinless boson with wave vector $\boldsymbol{k}$ and orbital angular momentum $\boldsymbol{\ell}$ is incident on another spinless boson initially at rest in the medium. General expressions for the cross-sections, including the total (σ_{T}) and viscosity (σ_η) cross-sections, are given by [16–20]:

$$\sigma_{\mathrm{T}} = \frac{8\pi}{k^2} \sum_{\ell(\text{even})}^{\infty} (2\ell + 1) \sin^2\left(\delta_\ell^E(k)\right), \tag{1}$$

$$\sigma_\eta = \frac{4\pi}{k^2} \sum_{\ell(\text{even})}^{\infty} \frac{(\ell+1)(\ell+2)}{\left(\ell+\frac{3}{2}\right)} \sin^2\left(\delta_{\ell+2}^E(k) - \delta_\ell^E(k)\right). \tag{2}$$

The average cross-sections ($\langle\sigma_{\mathrm{T}}\rangle$, $\langle\sigma_\eta\rangle$) are calculated according to [21]:

$$\langle\sigma\rangle = (k_{\mathrm{B}}T)^{-(p+1)} \int_0^{\infty} \sigma(E) E^P e^{(-E/k_\beta T)} dE, \tag{3}$$

k_{B} being Boltzmann's constant. For $p = 1$, this corresponds to the average total cross-section $\langle\sigma_{\mathrm{T}}\rangle$; for $p = 3$, it reduces to the average viscosity cross-section $\langle\sigma_\eta\rangle$.

Occasionally, we shall use a "natural" system of units, such that $\hbar = 2m = k_{\mathrm{B}} = 1$, m being the atomic mass and $\hbar$ Dirac's constant ($= h/2\pi$). The conversion factor is $\hbar^2/2m = 1.2162494$K Å^2.

The classical second virial coefficient $B_{\mathrm{cl}}(T)$ is given by [22, 23]:

$$B_{\mathrm{cl}}(T) = 2\pi \int_0^{\infty} \left[1 - e^{-\beta V(r)}\right] r^2\, dr. \tag{4}$$

The expression $\left(1 - e^{\beta V(r)}\right)$ is the well-known Mayer function, β being the inverse temperature [in our natural units] and $V(r)$ the interatomic potential. Clearly, the sole input in calculating $B_{\mathrm{cl}}(T)$ is $V(r)$.

On the other hand, the quantum second virial coefficient $B_{\mathrm{q}}(T)$ is given by the well-known Beth–Uhlenbeck formula [24, 25]:

$$B_{\mathrm{q}}(T) = -\frac{\lambda^3}{2^{5/2}} - 2^{3/2}\lambda^3 \sum_{E_{\mathrm{B}}} \left(e^{-\beta E_{\mathrm{B}}} - 1\right)$$

$$-\frac{2^{3/2}\lambda^5}{\pi^2} \int_0^{\infty} dk\, k \sum_{\ell(\text{even})}^{\infty} (2\ell+1)\, \delta_\ell^E(k)\, e^{-\beta E(k)}. \tag{5}$$

Here λ is the thermal de Broglie wavelength, E_{B} denotes bound-state energies and $\delta_\ell^E(k)$ is the effective ℓ-partial phase shift corresponding to energy $E(k) = \hbar^2 k^2/2m$. The first term on the right-hand side is the "ideal Bose gas" term which diminishes with increasing temperature; it depends on the statistics, but not on the interaction. The second represents the contribution of bound states in the system; it is related to its discrete energy levels. However, this term can be neglected [26], as shown below. The third term represents the contribution of scattering states; it is the major term in $B_{\mathrm{q}}(T)$ [12, 14].

2.2. GMF T-matrix

The starting point in computing B_{q}, then, is the determination of δ_ℓ^E. This can be accomplished by solving the GMF integral equation for the T-matrix, using a matrix-inversion technique.

This matrix is given by a Bethe-Salpeter-like equation [10, 11, 27]:

$$T(\boldsymbol{p}, \boldsymbol{p}'; s, \boldsymbol{P}, \beta) = u(|\boldsymbol{p} - \boldsymbol{p}'|) - (2\pi)^{-3}$$

$$\times \int d\boldsymbol{k}\, u(|\boldsymbol{p} - \boldsymbol{k}|) \left[g_0(k, s)\, Q(\boldsymbol{k}, \boldsymbol{P}, \beta)\right.$$

$$\left. - g_0^+(k, s)\, \bar{Q}(\boldsymbol{k}, \boldsymbol{P}, \beta)\right] T(\boldsymbol{k}, \boldsymbol{p}'; s, \boldsymbol{P}, \beta). \tag{6}$$

Here p and p' are the relative incoming and outgoing momenta; P is the center-of-mass momentum. The operator $u \equiv \frac{2m_{\mathrm{r}}V}{\hbar^2} \equiv \frac{1}{2}V$ [in natural units], m_{r} being the reduced mass of the Ar interacting pair: $m_{\mathrm{r}} = \frac{1}{2}m$, and V is the Fourier transform of a static central two-body potential. The free two-body Green function $g_0(s)$ is specified by $g_0(\boldsymbol{k}, s) \equiv \frac{1}{k^2 - s - \mathrm{i}\eta}$, η being a positive infinitesimal in the scattering region ($s > 0$) and zero otherwise, and the parameter s is the total energy of the interacting pair in the center-of-mass frame, given by

$$s \equiv 2\mu\left(2P_0 - \frac{P^2}{m}\right), \tag{7}$$

P_0 is the total energy of the pair and P^2 is the energy carried by the center of mass. For a many-bosonic system,

the operator $Q\left(\bar{Q}\right)$ is the product of two distributions as follows [12, 13, 28]:

$$Q\left(k, P, \beta\right) = \left(1 + n\left(|\boldsymbol{k} - \boldsymbol{P}|\right)\right)\left(1 + n\left(|\boldsymbol{k} + \boldsymbol{P}|\right)\right), \quad (8)$$

$$\bar{Q}\left(k, P, \beta\right) = n\left(|\boldsymbol{k} - \boldsymbol{P}|\right)n\left(|\boldsymbol{k} + \boldsymbol{P}|\right). \quad (9)$$

where $n\left(\boldsymbol{k}\right)$ is the Bose–Einstein distribution, given by

$$n\left(\varepsilon\right) = \frac{1}{\mathrm{e}^{\beta(\varepsilon - \mu)} - 1}, \quad (10)$$

ε being the single-particle energy.

The chemical potential μ is given by [29]:

$$\mu = k_{\mathrm{B}} T \ln\left(\frac{n}{n_{\mathrm{q}}}\right), \quad (11)$$

n_{q} is the quantum concentration given by $n_{\mathrm{q}} = \left(\frac{m k_{\mathrm{B}} T}{2\pi \hbar^2}\right)^{3/2}$.

Upon partial-wave decomposition, Eq. (6) takes the form [11]:

$$T_\ell\left(\boldsymbol{p}, \boldsymbol{p}'; s, \boldsymbol{P}, \beta\right) = u_\ell\left(|\boldsymbol{p} - \boldsymbol{p}'|\right) - (2\pi)^{-2}$$

$$\times \int_0^\infty k^2\, \mathrm{d}\boldsymbol{k}\, u_\ell\left(|\boldsymbol{p} - \boldsymbol{k}|\right)\left[g_0\left(k, s\right) Q\left(\boldsymbol{k}, \boldsymbol{P}, \beta\right)\right.$$

$$\left. - g_0^+\left(k, s\right) \bar{Q}\left(\boldsymbol{k}, \boldsymbol{P}, \beta\right)\right] T_\ell\left(\boldsymbol{k}, \boldsymbol{p}'; s, \boldsymbol{P}, \beta\right). \quad (12)$$

This equation represents the full-off-shell T-matrix pertaining to a relative partial wave ℓ, from which the on-energy-shell counterpart $T_\ell\left(\boldsymbol{p}, \boldsymbol{P}\right)$ is obtained directly by setting $\boldsymbol{p} = \boldsymbol{p}'$ and $s = p^2$. Clearly, in the free-scattering limit, $Q(\bar{Q}) \to 1(0)$; so that Eq. (6) reduces to the Lippmann–Schwinger t-matrix.

The parametrized $T_\ell\left(p; P; \beta\right)$ can be expressed in terms of real effective many-body shifts $\delta_\ell^E\left(p; P, \beta\right)$ according to [10, 11]:

$$T_\ell\left(p; P; \beta\right) = -\frac{2\pi}{p\left(Q\left(p; P, \beta\right) + \bar{Q}\left(p; P, \beta\right)\right)}$$

$$\times \left[\sin\left(2\delta_\ell^E\left(p; P, \beta\right)\right) + \mathrm{i}\left(1 - \cos\left(2\delta_\ell^E\left(p; P, \beta\right)\right)\right)\right], \quad (13)$$

so that

$$\delta_\ell^E\left(p; P, \beta\right) \equiv \tan^{-1}\frac{\mathrm{Im}T_\ell\left(p; P; \beta\right)}{\mathrm{Re}T_\ell\left(p; P; \beta\right)}. \quad (14)$$

$\mathrm{Im}T_\ell\left(p; P; \beta\right)$ and $\mathrm{Re}T_\ell\left(p; P; \beta\right)$ denote, respectively, the imaginary and real parts of $T_\ell\left(p; P; \beta\right)$, and are defined by

$$\mathrm{Re}T_\ell\left(p; P; \beta\right) = -\frac{2\pi}{p\left(Q\left(p; P, \beta\right) + \bar{Q}\left(p; P, \beta\right)\right)}$$

$$\times \sin\left(2\delta_\ell^E\left(p; P, \beta\right)\right), \quad (15)$$

$$\mathrm{Im}T_\ell\left(p; P; \beta\right) = -\frac{2\pi}{p\left(Q\left(p; P, \beta\right) + \bar{Q}\left(p; P, \beta\right)\right)}$$

$$\times \left(1 - \cos\left(2\delta_\ell^E\left(p; P, \beta\right)\right)\right). \quad (16)$$

The two-body potential representing the Ar–Ar interaction is taken in the present work as the HFD-B3 potential [15]. This is because the HFD-B3 potential characterizes accurately the properties which "feel" the well, together with the low and very high repulsive regions, of the potential. However, it should be mentioned that this potential fails to predict the transport properties of the

gas in the 1600–7000 K temperature range [15] which is well outside the present range. This potential is given by

$$V\left(r\right) = \varepsilon V^*\left(x\right), \quad (17)$$

$$V^*\left(x\right) = A\exp\left(-\alpha x + \beta x^2\right) - F\left(x\right)\sum_{j=0}^{2} c_{2j+6}\big/x^{2j+6},$$

$$F\left(x\right) = \begin{cases} \exp\left(-\left(\left(\frac{D}{x} - 1\right)^2\right)\right), & x < D \\ 1, & x > D \end{cases}$$

$x \equiv \frac{r}{r_m}$, $r_{\mathrm{m}} = 3.761$ Å, $A = 1.13211845$, $\alpha = 9.00053441$, $\beta = 2.60270226$, $D = 1.04$, $C_6 = 1.09971113$, $C_8 = 0.54511632$; $C_{10} = 0.39278653$, $\varepsilon/k_{\mathrm{B}} = 143.25$ K.

The principal features of the interatomic argon potential are: (i) a strongly-repulsive, short-range component arising from the Pauli exclusion principle as the electronic clouds of the two interacting atoms begin to overlap strongly; (ii) a weakly-attractive tail, thanks to Van der Waals' forces, which can be viewed either as a multipole expansion reflecting the interaction between the polarization fields associated with the interacting atoms or, in field-theoretic language, exchange of long-wavelength phonons; (iii) a minimum in between denoting equilibrium. This is the same as in other inert atomic systems — including helium, lithium, neon and sodium, among others.

The T-matrix takes into account only "ladder" diagrams; the long-range "ring" diagrams are not included, nor is the "self-energy insertion". Cumulative experience [12] indicates that this is justified in gaseous, relatively low-dense and weakly-interacting systems, such as ours.

3. Results and discussion
3.1. Effective cross-sections

The effective Ar–Ar total, viscosity and average cross-sections were calculated using the HFD-B3 potential, according to Eqs. (1)–(3), respectively. It was found necessary to include partial waves up to $\ell = 36$, so as to obtain results accurate to better than $\approx 0.5\%$. Our results are summarized in Figs. 1–5 and Tables I–III.

Figure 1 shows the behavior of the effective total cross-section σ_{T}, together with the even ℓ-wave components $\sigma_\ell (\ell = 0, 2, 4, 6, 8, 10)$, as functions of the relative momentum k. There exists a minima-and-maxima structure in σ_{T}. The peaks in σ_{T} imply a resonance-like behavior. The resonances are essentially bound states, but with shorter lifetimes; they are quasi-bound states. These arise because the repulsive angular-momentum barrier $\approx \frac{\ell(\ell+1)}{r^2}$ "screens" the short-range repulsive part of the interatomic potential, thereby allowing the interacting particles to "see" in effect more attraction. For $k \approx 0.125$ Å^{-1}, S-wave $(\ell = 0)$ scattering dominates. With increasing k, σ_0 tends to decrease, whereas the contribution of higher ℓ-waves to the scattering increases. Specifically, D-wave $(\ell = 2)$ scattering for $k \approx 0.338$ Å^{-1} dominates; so does G-wave $(\ell = 4)$ scattering for $k \approx 0.573$ Å^{-1}. The I wave $(\ell = 6)$ is the
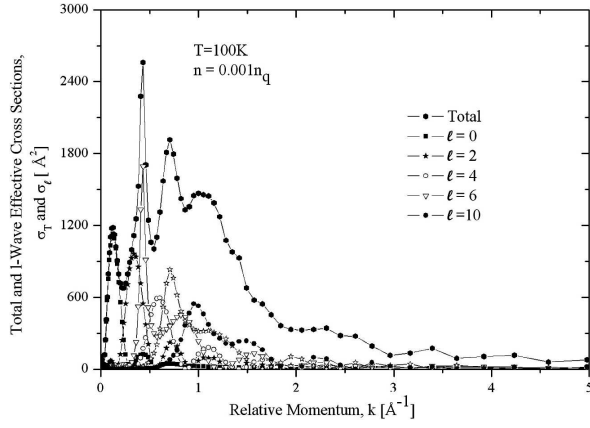
Fig. 1. The ℓ-wave effective cross-sections σ_ℓ [Å^2], $\ell = 0, 2, 4, 6, 8, 10$, and the total cross-section σ_T [Å^2] for Ar–Ar scattering as functions of relative momentum k [Å^{-1}].

most significant partial wave contributing to the total cross-section for $k \approx 0.4$ Å^{-1}; so is the ($\ell = 8$) wave for $k \approx 0.711$ Å^{-1} and the ($\ell = 10$) wave for $k \approx 0.950$ Å^{-1}.

TABLE I

The relative momentum at resonance k_R and the binding energy E_R [K] of the weakly-bound (Ar)$_2$-dimer for various ℓ.

ℓ	k_R [Å^{-1}]	E_R [K]
0	0.125	0.019
2	0.338	0.139
4	0.573	0.399
6	0.433	0.228
8	0.710	0.613
10	0.950	1.10

The energies of all resonances E_R can be determined from $E_R = \left(\frac{\hbar^2 k_R^2}{m}\right)$, k_R being the relative momentum at resonance; they are given in Table I. Substituting these in the second term on the right-hand side of Eq. (5), one concludes that this term is indeed negligible.

TABLE II

The relative momentum k_{min} and the binding energy E_{min} [K] of the weakly-bound (Ar)$_2$-dimer for various ℓ.

ℓ	k_{min} [Å^{-1}]	E_{min} [K]
0	0.295	0.106
2	0.573	0.399
4	0.863	0.906
6	0.574	0.400

The minimum is evidence for the atomic Ramsauer–Townsend effect [30], occurring in the collision between two bodies when the total cross-section is a minimum and, therefore, the mobility is a maximum [31]. This minimum arises from a delicate balance between the attractive long-range and repulsive short-range interactions.

We have already encountered it in other atomic systems where we have analyzed it quite carefully [32]. It appears in electronic systems and in molecular ^{4}He–^{4}He [12, 13, 33, 34] as well as ^{3}He–^{3}He [12, 35]. Our results for E_{min} are presented in Table II.
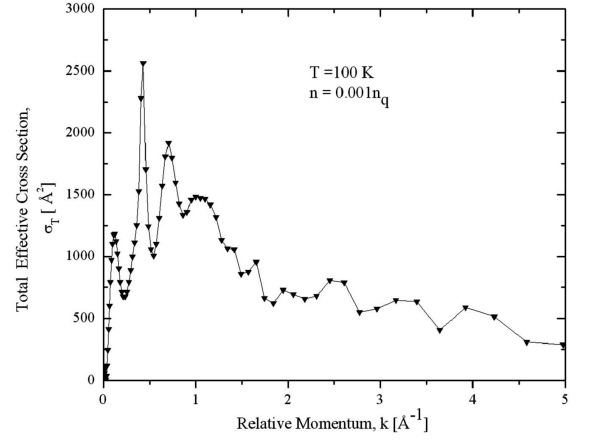

Fig. 2. The effective total cross-section σ_T [Å^2] for Ar–Ar scattering as a function of relative momentum k [Å^{-1}].

In the high-energy region, there are undulations in σ_T. These originate from the indistinguishability of the Ar atoms, which are scattered mainly by the repulsive part of the potential [36, 37]. Because the kinetic-energy part is much larger than the interaction part, the amplitude of the undulations decreases, to a first approximation; as the inverse of the relative velocity of the colliding atoms [36, 38]. Figure 2 displays σ_T as a function of k at $T = 100$ K.

TABLE III

The S-wave scattering length a_0 [Å] and cross-section $\sigma_T(0)$ [Å^2] at different T [K] for two different n.

| T [K] | $n = 0.001 n_q$ | | $n = 0.01 n_q$ | |
	a_0 [Å]	$\sigma_T(0)$ [Å^2]	a_0 [Å]	$\sigma_T(0)$ [Å^2]
90	−2.04	105.10	206.50	9.16×10^5
100	−2.05	105.70	192.70	1.05×10^5
105	−2.06	105.20	186.90	8.63×10^5
120	-2.05	105.26	172.48	7.37×10^5

Table III exhibits the relation between the number density n and the S-wave scattering length a_0 at different T. It is noted that a_0 and $\sigma_T(0)$ depend on n, but hardly on T: at low n, $a_0 < 0$ (attractive case); whereas at high n, $a_0 \gg 0$ (weakly-bound, fragile case). Figure 3 represents the effective viscosity cross-section σ_η as a function of k; σ_η has the same overall behavior as σ_T.

The average total cross-section $\langle\sigma_T\rangle$ tends to decrease as T increases at the same value of n. This is evident in plots of $\langle\sigma_T\rangle$ vs. T, Fig. 4. Also, it is clear that $\langle\sigma_T\rangle$ is nearly constant at low n, but increases at high n. The average viscosity cross-section $\langle\sigma_\eta\rangle$ has the same general behavior as $\langle\sigma_T\rangle$ (Fig. 5).
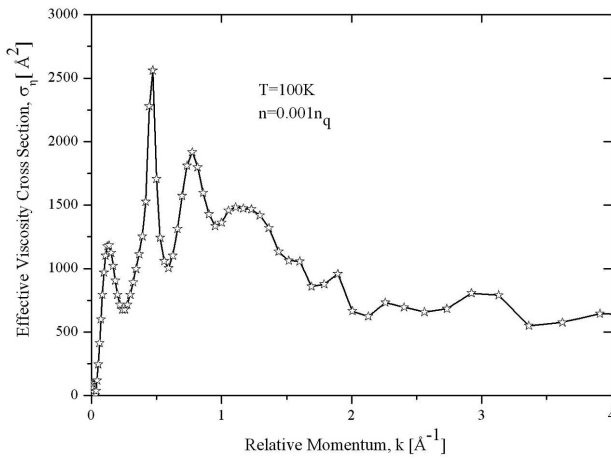
Fig. 3. The effective viscosity cross-section σ_η [Å^2] for Ar–Ar scattering as a function of relative momentum k [Å^{-1}].
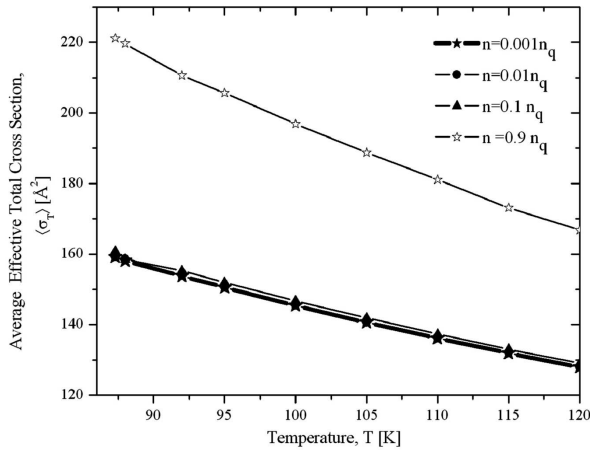

Fig. 4. The average effective total cross-section $\langle\sigma_T\rangle$ [Å^2] for Ar-Ar scattering as a function of temperature T [K] for different number densities n.
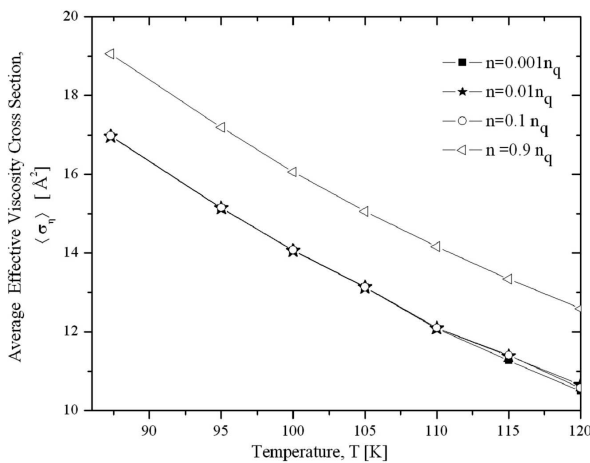

Fig. 5. The average effective viscosity cross-section $\langle\sigma_\eta\rangle$ [Å^2] for Ar-Ar scattering as a function of temperature T [K] for different number densities n.

3.2. Second virial coefficient

Our results for the classical and quantum second virial coefficients are summarized in Figs. 6,7 and Tables IV,V for the HFD-B3 potential. These coefficients were calculated in the T-range 87.3–120 K. Clearly B_{cl} and B_q are predominantly negative; but B_{cl} and B_q become less negative as T increases.
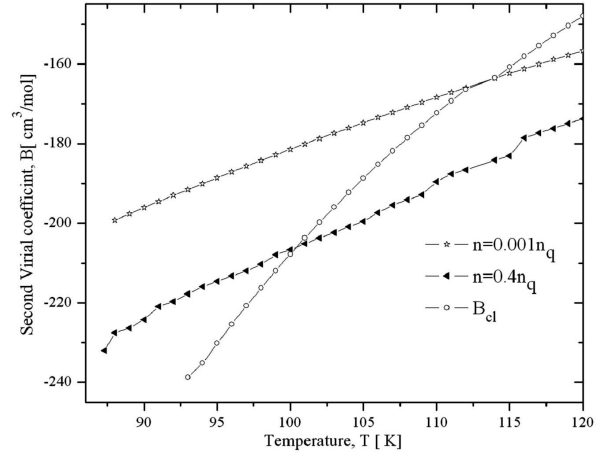

Fig. 6. The quantum second virial coefficient B_q [cc/mole] as a function of temperature T [K] for different number densities n. The classical second virial coefficient B_{cl} is also plotted for comparison purposes.
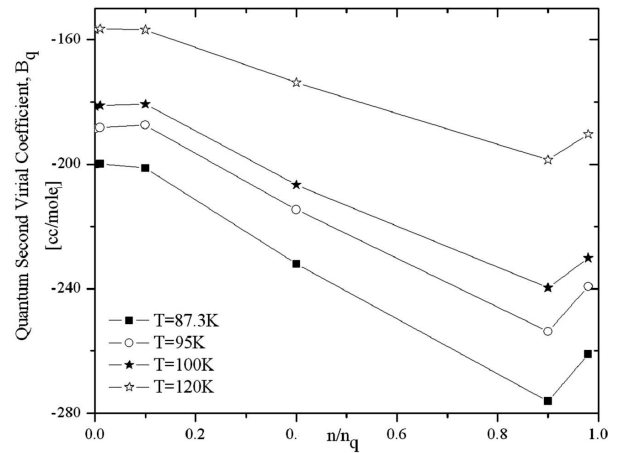

Fig. 7. The quantum second virial coefficient B_q [cc/mole] as a function of n/n_q at different temperatures T [K].

The quantum second virial coefficient B_q was calculated for different n and compared with B_{cl} as shown in Fig. 6. From this figure it is noted that B_{cl} and B_q falls rapidly as T is reduced towards the lower limit of this range. For low T, the mean energies of the atoms in the gas are of the same order of magnitude as the depth of the potential well, resulting in an increase in the attractive forces between the interacting atoms; these spend most of their time in the attractive region of the potential. This results in a decrease in the gas pressure which leads

to a negative $B(T)$. For high T, the average energies of the atoms increase and become large in comparison to the maximum energy of attraction. Therefore, the predominant contribution to $B(T)$ arises from the repulsive portion of the potential. This causes an increase in the gas pressure and, hence, $B(T)$ becomes less negative [39].

Figure 7 shows that B_q starts to decrease as n increases, reaching a minimum then increasing again. The minimum value B_{qmin} increases (becomes less negative) with increasing T. At relatively high T, particles may collide with such a great force that some interpenetration is possible. When this occurs, the increase in n causes a decrease in B_q [39].

TABLE IV

The quantum second virial coefficient B_q [cc/mole] at different T [K]. Some previous results are included for comparison purposes.

T [K]	$B_q(T)_{at}$ $n=0.0$ (LS)	$B_q(T)_{at}$ $n=0.001nq$	$B_q(T)_{at}$ $n=0.4nq$	$B(T)_{th}$ [5]	$B(T)_{exp}$ [40]	$B(T)_{th}$ [7]
88	-199.73	-199.24	-227.50	-231.20	-239.10	
90	-196.56	-196.10	-224.20	-221.67		-215.22
92	-193.48	-193.04	-219.60	-212.77	-219.30	
94	-190.47	-190.05	-215.90	-204.44		
96	-187.52	-187.12	-213.20	-196.63	-202.00	
98	-184.64	-184.27	-210.30	-189.29		
100	-181.83	-181.47	-206.60	-182.37	-186.80	-180.09
102	-179.07	-178.73	-203.70	-175.86		
104	-176.38	-176.06	-200.90	-169.70	-173.30	
106	-173.75	-173.44	-197.30	-163.88		
108	-171.18	-170.89	-194.10	-158.37	-161.20	
110	-168.66	-168.39	-189.50	-153.14		-152.39
112	-166.21	-165.98	-186.60		-150.50	
115	-162.62	-162.34	-183.10	-141.17		
116	-161.45	-161.20	-178.60		-140.80	
120	-156.89	-156.66	-173.80	-130.58	-132.00	-130.32

Table IV includes a comparison of our results to experimental and other theoretical values. Clearly, the present results are comparable to those. In particular, the GMF results (at high n) show good agreement with previous results at $T < 94$ K, whereas the LS results show good agreement at $T > 94$ K. However, the GMF formalism should be more accurate than the LS formalism because the latter completely ignores the medium! We therefore humbly believe that the present calculations merit a new experimental investigation of B for Ar gas. The results of Ref. [5] were calculated classically; quantum corrections were then added.

Argon is expected to be a classical gas in the present T-range — unlike helium gas which exhibits a strong quantum behavior at low T [12]. There is more than one way of characterizing the "quantumness" of a system. One such measure is the quantum parameter η [41]:

$$\eta = \left(\hbar^2/m\varepsilon r_m^2\right)^{1/2}. \tag{18}$$

This is in effect the ratio of the kinetic energy at zero T to potential energy. For Ar, $r_m = 3.761$ Å; at $\varepsilon/k_B = 143.25$ K, $\eta = 0.02$.

Another measure of quantumness is the thermal de Broglie wavelength λ that should be compared to the interparticle distance $(1/n)^{1/3}$ at $n > n_{Bmin} = 0.9n_q$. B_{qmin} and the corresponding values of n, n_{Bmin}, $(1/n)^{1/3}$ and λ are listed in Table V. It is noted that the minimum of B_q occurs when the interparticle distance has the largest value.

TABLE V

B_{qmin} [cc/mol] and the corresponding, n_q, n_{Bmin}, $(1/n)^{1/3}$ and λ for different T [K].

T [K]	B_{qmin} [cc/mol]	$n_q \times 10^{31}$ [atoms/m³]	$n_{Bmin} \times 10^{31}$ [atoms/m³]	$(1/n)^{1/3}$ [Å]	λ [Å]
87.3	–276.1	38.61	34.75	0.306	0.296
90	–266.9	40.42	36.38	0.302	0.291
95	–253.8	43.83	39.45	0.294	0.284
100	–239.7	47.34	42.60	0.286	0.276
120	–199.0	62.23	56.00	0.2613	0.252

From this table, it is concluded that Ar gas exhibits small quantum effects in the T-range considered.

3.3. Pressure–volume–temperature (P–V–T) behavior

The "virial equation of state" is given by [22]:

$$\frac{P}{nk_BT} = 1 + nB_q. \tag{19}$$

The B_q-dependence on T can readily be obtained by applying least-squares fitting to the polynomial

$$B_q = A + BT + CT^2 + DT^3 + ET^4, \tag{20}$$

where A, B, C, D, and E are listed in Table VI for different n.

TABLE VI

The parameters of B_q, calculated for different n.

n/n_q	A $\left[\frac{cc}{mol}\right]$	B $\left[\frac{cc}{(mol\ K)}\right]$	C $\left[\frac{cc}{(mol\ K^2)}\right]$	D $\left[\frac{cc}{(mol\ K^3)}\right]$	E $\left[\frac{cc}{(mol\ K^4)}\right]$
0.001	-437.816	4.184	-0.02096	5.123×10^{-5}	-3.658×10^{-8}
0.01	-369.166	1.657	0.01422	-1.670×10^{-4}	4.7052×10^{-7}
0.1	2562.201	-116.146	1.77470	-0.01177	2.8922×10^{-5}
0.4	-10286.016	381.222	-5.42892	0.03438	-8.133×10^{-5}
0.9	4770.572	-195.639	2.74791	-0.01659	3.6693×10^{-5}

The results for B_q and the corresponding fitted equations are plotted in Fig. 8 for the HFD-B3 potential. The agreement is excellent between the fitted curves and the calculated values of B_q in the present T-range for different n.

The P–T curves in Fig. 9 indicate that P increases with increasing T, n being held fixed. Figure 10, on the other hand, shows that P reaches a maximum then decreases with increasing n. This is because the interatomic repulsive forces cause P to increase rapidly from A to B; whereas the attractive forces cause P to decrease equally rapidly from B to C (gas–liquid transition) [42]. The values of P, T, and n in both figures are based on Table VII. Our results are compared in Table VIII to experimental values.
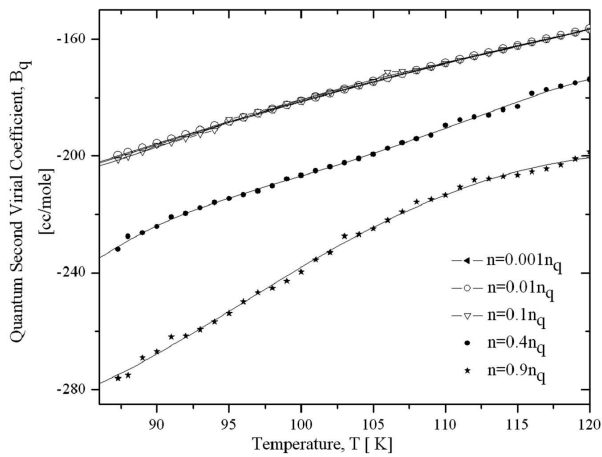
Fig. 8. The calculated quantum second virial coefficient B_q [cc/mole] values and their fitting equations versus temperature T [K] for different number densities n.
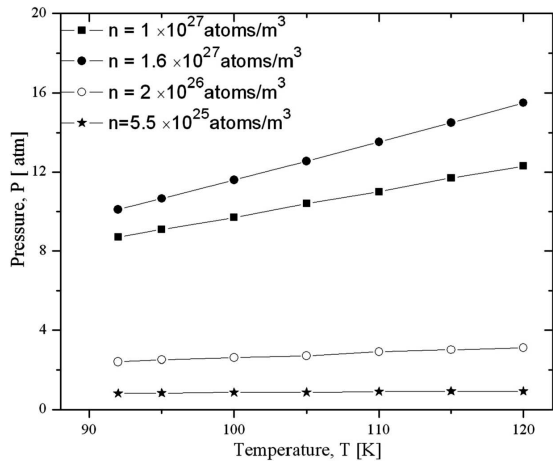

Fig. 9. The pressure P [atm] as a function of temperature T [K] for different number densities n [atoms/m³].
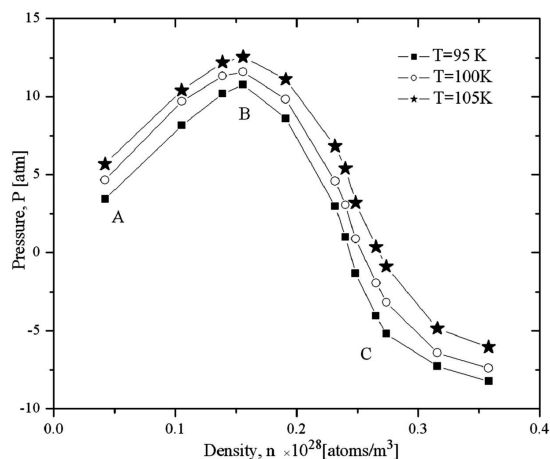

Fig. 10. The pressure P [atm] as a function of number density n [atoms/m³] at different temperatures T [K].

TABLE VII

The pressure P [atm] as a function of temperature T [K] for different number densities n [atoms/m³], using the virial equation of state.

T [K]	n [atoms/m³]						
	2×10^{25}	5.5×10^{25}	2×10^{26}	10^{27}	1.6×10^{27}	2×10^{27}	8×10^{27}
	P [atm]						
87.3	0.230	0.79	2.25	8.0	9.86	8.7	-200.8
92	0.259	0.82	2.40	8.7	10.1	9.0	-194.8
95	0.274	0.84	2.50	9.1	10.7	9.9	-194.2
100	0.288	0.865	2.60	9.7	11.6	11.0	-192.7
105	0.302	0.869	2.70	10.4	12.5	12.0	-191.4
110	0.317	0.91	2.90	11.0	13.5	13.4	-184.4
115	0.331	0.92	3.00	11.7	14.5	14.6	-182.0
120	0.346	0.928	3.10	12.3	15.5	15.9	-173.5

TABLE VIII

The pressure P [atm] as a function of temperature T [K]; the number density $n = 2 \times 10^{26}$ atoms/m³. Some previous theoretical results are included for comparison purposes.

T [K]	P [atm]	Previous data
92	2.4	1.6 atm; $n = 1.3 \times 10^{26}$ m⁻³ [40]
95	2.5	2.1 atm; $n = 1.7 \times 10^{26}$ m⁻³ [40]
100	2.6	3 atm; $n = 2.4 \times 10^{26}$ m⁻³ [42]
110	2.9	3 atm; $n = 2.1 \times 10^{26}$ m⁻³ [42]
120	3.1	3 atm; $n = 1.9 \times 10^{26}$ m⁻³ [42]

The critical physical quantities n_c and V_c as well as the maximum pressure P_{max} are listed in Table IX at different T. Figure 11 shows P as a function of V for different T. It is noted that if the system is compressed, V decreases until it reaches a critical value ($V_c \approx 6.25 \times 10^{28}$ m³/atom) at $P_{max} \approx 10.66$ atm when $T = 95$ K. If V is decreased a little below V_c by compression to a pressure a little above P_{max}, the system begins to collapse; V and P decrease at the same time,
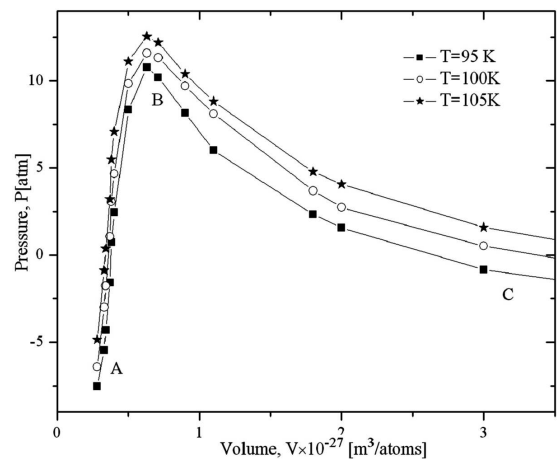

Fig. 11. The pressure P [atm] as a function of volume V [m³/atom] at different temperatures T [K].

T being held fixed. As expected, the system undergoes a phase (gas–liquid) transition. Our value for V_c (6.25×10^{-28} m^3/atom) is reasonably close to that obtained previously (0.0860 L/mol $\approx 1.43 \times 10^{-28}$ m^3/atom) [42].

TABLE IX

The critical number density n_c [atoms/m^3] at the maximum pressure $P_{\max}$ [atm] for different temperatures T [K], calculated from the virial equation of state.

T [K]	n_c [atoms/m^3]	V_c [m^3/atoms]	$P_{\max}$ [atm]
95	1.6×10^{27}	6.25×10^{-28}	10.66
100	1.6×10^{27}	6.25×10^{-28}	11.59
105	1.6×10^{27}	6.25×10^{-28}	12.55

The equation of state was also used to calculate the following thermodynamic properties:

a) Internal energy U and enthalpy H

The internal energy U for Ar can be calculated via the following Eq. [6]:

$$\frac{U}{Nk_BT} = \frac{3}{2} + \frac{U^{ex}}{Nk_BT}. \tag{21}$$

Our results for U and their comparison to the experimental values [40] are shown in Fig. 12. It is noted that U increases as T increases since the repulsive forces increase.
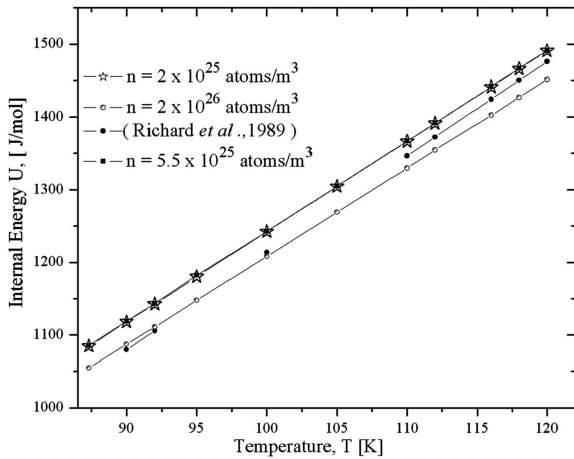

Fig. 12. The internal energy U [J/mol] as a function of temperature T [K] for two different number densities n. The experimental data [40] at $n \approx 5.5 \times 10^{25}$ atoms/m^3 are also shown.

The enthalpy H:

$$H = U + PV, \tag{22}$$

$$H = U + Nk_BT(1 + nB(T)). \tag{23}$$

Figure 13 displays our results for H and their comparison to the experimental values [40]. It is noted that H increases as T increases and as n decreases.

b) Helmholtz free energy F(N, V, T)

This is given by [43]:

$$F = Nk_BT\left[\ln\left(n\lambda^3\right) - 1 + nB(T)\right]. \tag{24}$$

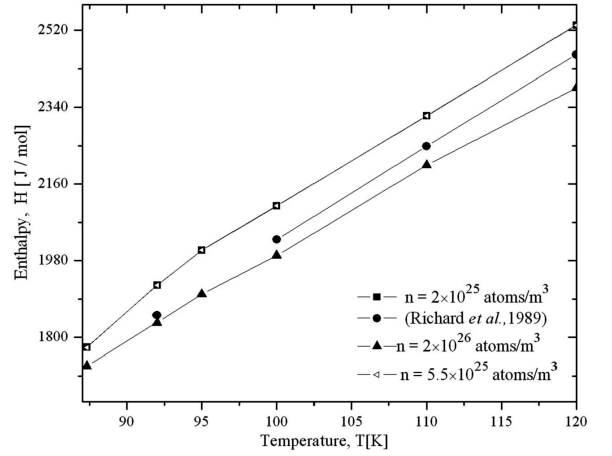Our results for F are illustrated in Fig. 14. It is noted

Fig. 13. The enthalpy H [J/mol] as a function of temperature T [K] for two different number densities n. The experimental data [40] are included for comparison purposes.

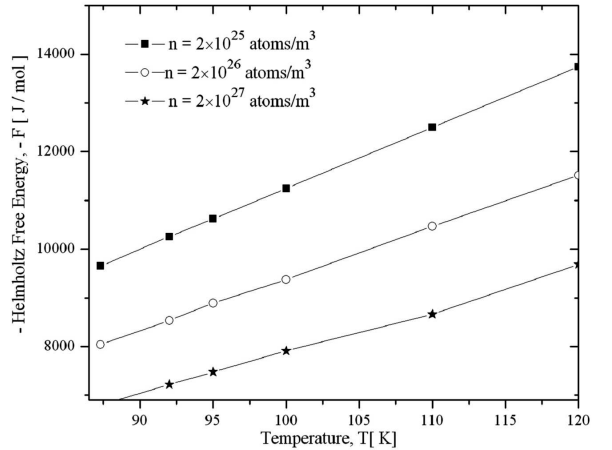that F increases as T increases and as n decreases.

Fig. 14. The Helmholtz free energy F [J/mol] versus temperature T [K] for three different number densities n.

c) Entropy S

This is defined as:

$$S = -\left(\frac{\partial F}{\partial T}\right)_V. \tag{25}$$

From Eq. (24):

$$S = Nk_B\left[\ln\left(n\lambda^3\right) - 1 + nB(T)\right] + \frac{3}{2}Nk_B$$

$$-nNk_BT\left(\frac{dB(T)}{dT}\right), \text{ or } S = -\frac{F}{T} + \frac{3}{2}Nk_B + \frac{U^{ex}}{T}. \tag{26}$$

Our results for S, together with the corresponding experimental data [40], are shown in Fig. 15. It is noted that S increases with increasing T and n.

d) Heat capacity C_V
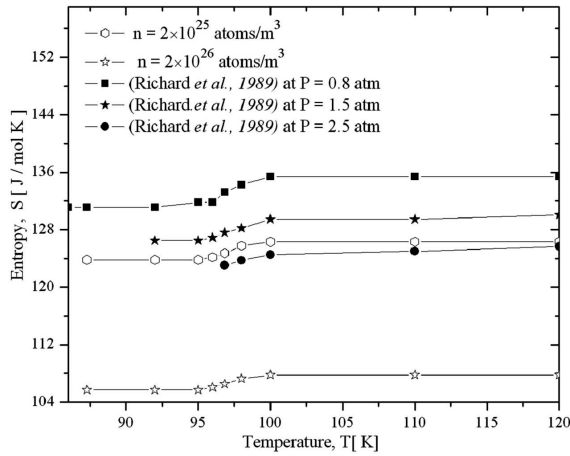
This is defined as:

Fig. 15. The entropy S [J/(mol K)] as a function of temperature T [K] for two different number densities n. The experimental data [40] are included for comparison purposes.

$$C_V = T\left(\frac{\mathrm{d}S}{\mathrm{d}T}\right)_V. \qquad (27)$$

From Eq. (26):

$$C_V = T\left[\frac{F}{T^2} - \frac{1}{T}\left(\frac{\mathrm{d}F}{\mathrm{d}T}\right)_V\right] - Nnk_{\mathrm{B}}T\left(\frac{\mathrm{d}B(T)}{\mathrm{d}T}\right)_V$$

$$-Nnk_{\mathrm{B}}T^2\left(\frac{\mathrm{d}^2B(T)}{\mathrm{d}T^2}\right)_V,$$

$$C_V = S + \frac{F}{T} + \frac{U^{\mathrm{ex}}}{T} - Nnk_{\mathrm{B}}T^2$$

$$\times\left(2C + 6DT + 12ET^2\right). \qquad (28)$$

Our results for C_V versus T are shown in Fig. 16. It is clear that C_V decreases as n increases, and that the gas becomes more and more ideal as n decreases, as expected on physical grounds.
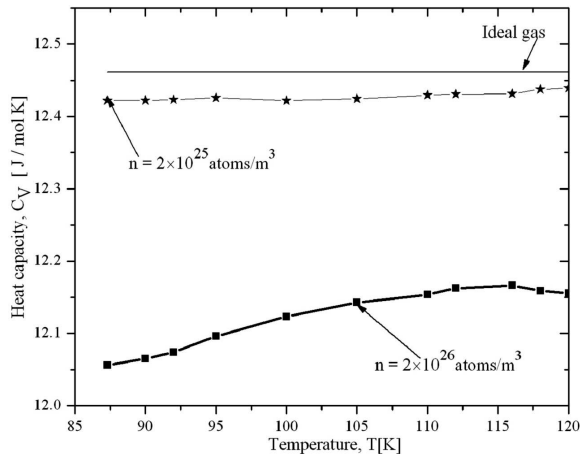

Fig. 16. The heat capacity C_V [J/(mol K)] versus temperature T [K] for two different number densities n.

4. Conclusion

In this paper, extensive results for Ar–Ar scattering in argon gas, using the GMF formalism, have been presented in the temperature range 87.3–120 K.

These results include the effective total and viscosity cross-sections as well as the average cross-sections and the quantum second virial coefficient. The calculations have been undertaken using the HFD-B3 potential. There is a minima-and-maxima structure in σ_{T}. The peaks in σ_{T} imply a resonance-like behavior. The resonances are essentially bound states, but with shorter lifetimes. These arise because the repulsive angular-momentum barrier $\sim \frac{\ell(\ell+1)}{r^2}$ "screens" the short-range repulsive part of the interatomic potential, thereby allowing the interacting particles to "see" more attraction.

The minimum is evidence for the Ramsauer–Townsend effect, occurring in the collision between two particles when the total cross-section is a minimum and, therefore, the mobility is a maximum.

In the quantum regime, it is concluded that B_{q} increases as T increases. B_{q} is nearly constant at low n, but starts to decrease as n increases, reaching a minimum then increasing again. Clearly, Ar gas exhibits small quantum effects in the temperature range considered.

The virial equation of state for Ar gas is constructed using the quantum second virial coefficient. The P–V–T behavior is carefully investigated, from which the phase (gas–liquid) transition is predicted.

The thermodynamic properties of Ar gas have been determined using this equation of state. It is concluded that, as expected, the gas becomes more and more ideal as n decreases. Our calculated results for the internal energy, enthalpy and entropy are in good agreement with experimental data.

There are quite a few problems that one can pursue starting with the present work. A first problem is the calculation of the various cross-sections of other atomic gases, such as Kr, as well as Ar–Ne and other inert gas mixtures. A second problem is the calculation of the inverse Fourier transform of the T-matrix. This transform represents the effective interaction in configuration space and can shed further light on the properties of the system. A third problem is the computation of the scattering properties of low-dimensional atomic gases (i.e., in confined geometries). A final problem is the systematic investigation of the "interface" between classical and quantum regimes in various atomic gases for different temperature and pressure ranges.

References

[1] F. Mozaffari, *J. Phys. Chem. Electrochem.* **2**, 2109 (2011).

[2] K. Gilles, *Weld. Des. Fabric.* **11**, 12 (2006).

[3] A.E. Nasrabad, R. Laghaei, U.K. Deiters, *J. Chem. Phys.* **121**, 6423 (2004).

[4]   A.E. Nasrabad, R. Laghaei, *J. Chem. Phys.* **125**, 084510 (2006).

[5]   E. Vogel, B. Jäger, R. Hellmann, E. Bich, *Mol. Phys.* **108**, 3335 (2010).

[6]   F. Mozaffari, Z.Z. Sharabadi, *J. Phys. Chem. Electrochem.* **1**, 139 (2011).

[7]   A.L. Gosman, R.D. McCarty, J.G. Hust, *National Standard Reference Data Series — National Bureau of Standards* 27, 1969.

[8]   Ch. Tegeler, R. Span, W. Wagner, *J. Phys. Chem. Ref. Data* **28**, 779 (1999).

[9]   F. Aitken, N. Bonifaci, A. Denat, F. Volino, arXiv:1504.00633v1, 2015.

[10] H.B. Ghassib, R.F. Bishop, M.R. Strayer, *J. Low Temp. Phys.* **23**, 393 (1976).

[11] R.F.Bishop, H.B.Ghassib, M.R. Strayer, *Phys. Rev. A* **13**, 1570 (1976).

[12] B.R. Joudeh, A.S. Sandouqa, H.B. Ghassib, M.K. Al-Sugheir, *J. Low Temp. Phys.* **161**, 348 (2010).

[13] H.B. Ghassib, A.S. Sandouqa, B.R. Joudeh, S.M. Mosameh, *Canad. J. Phys.* **92**, 997 (2014).

[14] S.M. Mosameh, A.S. Sandouqa, H.B. Ghassib, B.R. Joudeh, *J. Low Temp. Phys.* **175**, 523 (2014).

[15] R.A. Aziz, M.J. Slaman, *J. Chem. Phys.* **92**, 1030 (1990).

[16] S. Geltman, *Topics in Atomic Collision Theory*, Krieger Publ. Co., Florida 1997.

[17] E. Merzbacher, *Quantum Mechanics*, 3rd ed., Wiley, New York 1998.

[18] R.J. Kanzleiter, D.P. Stotler, C.F.F. Karney, D. Steiner, *Phys. Plasmas* **7**, 5064 (2000).

[19] M.J. Wright, D. Bose, G.E. Palmer, E. Levin, *AIAA J.* **43**, 2558 (2005).

[20] B.R. Joudeh, *Physica B Condens. Matter* **421**, 41 (2013).

[21] M.J. Jamieson, A. Dalgarno, J.N. Yukich, *Phys. Rev. A* **46**, 6956 (1992).

[22] R.P. Feynman, *Statistical Mechanics*, Benjamin, Reading, MA 1992.

[23] E.V.L. Mello, J.J. Rehr, O.E. Vilches, *Phys. Rev. B* **28**, 3759 (1983).

[24] E. Beth, G.E. Uhlenbeck, *Physica 3* **8**, 729 (1936).

[25] V. Seguin, H. Guignes, C. Lhuillier, *Phys. Rev. B* **36**, 141 (1987).

[26] S.P. Dardi, S.J. Dahler, *Theor. Chem. Acta* **82**, 117 (1992).

[27] A.L. Fetter, J.D. Walecka, *Quantum Theory of Many-Particle Systems*, McGraw-Hill, New York 1971.

[28] H.T. Stoof, M. Bijlsma, M. Houbiers, *J. Res. Natl. Inst. Stand. Technol.* **101**, 443 (1996).

[29] C. Kittel, H. Kroemer, *Thermal Physics*, Freeman, New York 1980.

[30] R. Feltgen, H. Pauly, F. Torello, H. Vehmeyer, *Phys. Rev. Lett.* **30**, 820 (1973).

[31] A.F. Borghesani, *J. Electrostat.* **53**, 89 (2001).

[32] A.S. Sandouqa, H.B. Ghassib, B.R. Joudeh, *Chem. Phys. Lett.* **490**, 172 (2010).

[33] W.A. Kampe, D.E. Oates, W. Schrader, H.G. Bennewitz, *Chem. Phys. Lett.* **18**, 323 (1973).

[34] T.K. Lim, S.Y. Larsen, *J. Chem. Phys.* **74**, 4997 (1981).

[35] R.S. Grace, W.M. Pope, D.L. Johnson, J.G. Skofronick, *Phys. Rev. A* **14**, 1006 (1976).

[36] P. Cantini, M.G. Dondi, G. Scoles, F. Torello, *J. Chem. Phys.* **56**, 1946 (1972).

[37] R. Feltgen, H. Krist, K.A. Köhler, H. Pauly, F. Torello, *J. Chem. Phys.* **76**, 2360 (1982).

[38] M.G. Dondi, G. Scoles, F. Torello, *J. Chem. Phys.* **51**, 392 (1969).

[39] P.J. Gans, *Phys. Chem. l* **25**, 0651 (1994).

[40] B.R. Stewart, T.R.J. Jacobsen, *J. Phys. Chem. Ref. Data* **18**, 639 (1989).

[41] L.H. Nosanow, *J. Low Temperature Phys.* **26**, 613 (1977).

[42] K.C. Kan, *Chin. J. Phys.* **17**, 32 (1979).

[43] F. Reif, *Fundamentals of Thermal Physics*, McGraw-Hill, New York 1965.